Synthesis, characterization and humidity sensing performance of chromium-substituted lithium–copper ferrites

Original
Synthesis, characterization and humidity sensing performance of chromium-substituted lithium–copper ferrites / Mandal, T., Kolekar, Y.D., Afre, R.A., Pugliese, D., Sonawane, K.M.. - In: SENSORS AND ACTUATORS. A, PHYSICAL. - ISSN 0924-4247. - 409:(2026). [10.1016/j.sna.2026.118061]

Publisher:
Elsevier B.V.

Published
DOI:10.1016/j.sna.2026.118061

Sensors & Actuators: A. Physical 409 (2026) 118061

Contents lists available at ScienceDirect

Sensors and Actuators: A. Physical

journal homepage: www.journals.elsevier.com/sensors-and-actuators-a-physical

Synthesis, characterization and humidity sensing performance of chromium-substituted lithium–copper ferrites

Tripti Mandal [a,b], Yesappa D. Kolekar [c], Rakesh A. Afre [d,e], Diego Pugliese [f,*], Kishor M. Sonawane [a,*]

[a] Department of Physics, Fergusson College (Autonomous), Savitribai Phule Pune University, Pune, Maharashtra 411004, India
[b] Department of Engineering Science, Zeal College of Engineering and Research, Narhe, Pune, Maharashtra 411041, India
[c] Department of Physics, Savitribai Phule Pune University, Pune, Maharashtra 411007, India
[d] School of Technology and Research, Dnyaan Prasad Global University, Sant Tukaram Nagar, Pimpri, Maharashtra 411018, India
[e] Department of First Year Engineering (Physics), Dr. D. Y. Patil Institute of Technology, Sant Tukaram Nagar, Pimpri, Pune 411018, Maharashtra, India
[f] Division of Applied Metrology and Engineering, National Institute of Metrological Research (INRiM), Torino 10135, Italy

ARTICLE INFO

Keywords:
Chromium-substituted ferrite
Spinel ferrite
Ceramic method
Humidity sensing properties
Response time
Recovery time

ABSTRACT

In this study, chromium-substituted lithium–copper ferrites with the nominal composition $Li_xCu_{1-x}Cr_yFe_{2-y}O_4$ ($x = 0.2$; $y = 0, 0.2, 0.4$) were prepared through the traditional ceramic route. X-ray diffraction (XRD) confirmed the formation of a single-phase cubic spinel structure (space group Fd3m), with crystallite sizes in the 37.1–37.2 nm range. The microstructural features—including particle shape, grain connectivity and porosity—were examined by scanning electron microscopy (SEM), while Fourier-transform infrared (FTIR) spectroscopy revealed characteristic ferrite absorption bands, with the most prominent features appearing between 420–497 cm^{-1} and 547–600 cm^{-1}. The optical response of the materials, evaluated by ultraviolet–visible (UV–Vis) spectroscopy, showed an increase in band gap upon chromium incorporation up to $y = 0.2$, followed by a reduction at $y = 0.4$. X-ray photoelectron spectroscopy (XPS) confirmed the presence of chromium in the lithium–copper ferrite system, while the specific surface area was evaluated using nitrogen adsorption–desorption measurements based on the Brunauer–Emmett–Teller (BET) method. Humidity-sensing behavior was assessed by monitoring the electrical resistance of the samples over a broad relative humidity interval (8.9–97%) at room temperature. All compositions exhibited the expected decrease in resistance with rising humidity and maintained stable performance over a 90-day period. Among the investigated ferrites, the $y = 0.2$ sample displayed the most favorable characteristics, offering response and recovery times of 77.8 s and 88.5 s, respectively. The experimental data over the entire humidity range were well fitted by the Freundlich adsorption isotherm, providing additional insight into the humidity sensing mechanism.

1. Introduction

Humidity is an environmental parameter that fluctuates continuously, making its precise monitoring essential. Reliable humidity control is crucial in applications ranging from human health and comfort to industrial processes and household technologies [1], since the amount of water vapor present in air influences numerous physical, chemical, and biological phenomena. When moisture levels rise beyond acceptable limits, both living conditions and manufacturing performance can deteriorate, underscoring the need for dependable sensing systems. For this reason, humidity sensors must offer high sensitivity over a broad operational range, minimal hysteresis during adsorption–desorption cycles, and fast response and recovery characteristics.

Humidity sensors encompass several operating principles, including capacitive, resistive, gravimetric, optical, quartz crystal microbalance, and surface acoustic wave designs [2–7]. Among these, capacitive and resistive configurations are the most widely implemented, with resistive sensors receiving particular attention because they typically offer high sensitivity and require relatively simple electronic circuitry. A broad range of functional materials—such as metal oxides, ceramics, polymers, and composite systems—has been explored for humidity detection [8–10]. Within this landscape, porosity is recognized as a critical

---

* Corresponding authors.
E-mail addresses: d.pugliese@inrim.it (D. Pugliese), kishor.sonawane@fergusson.edu (K.M. Sonawane).

https://doi.org/10.1016/j.sna.2026.118061
Received 13 December 2025; Received in revised form 13 May 2026; Accepted 30 May 2026

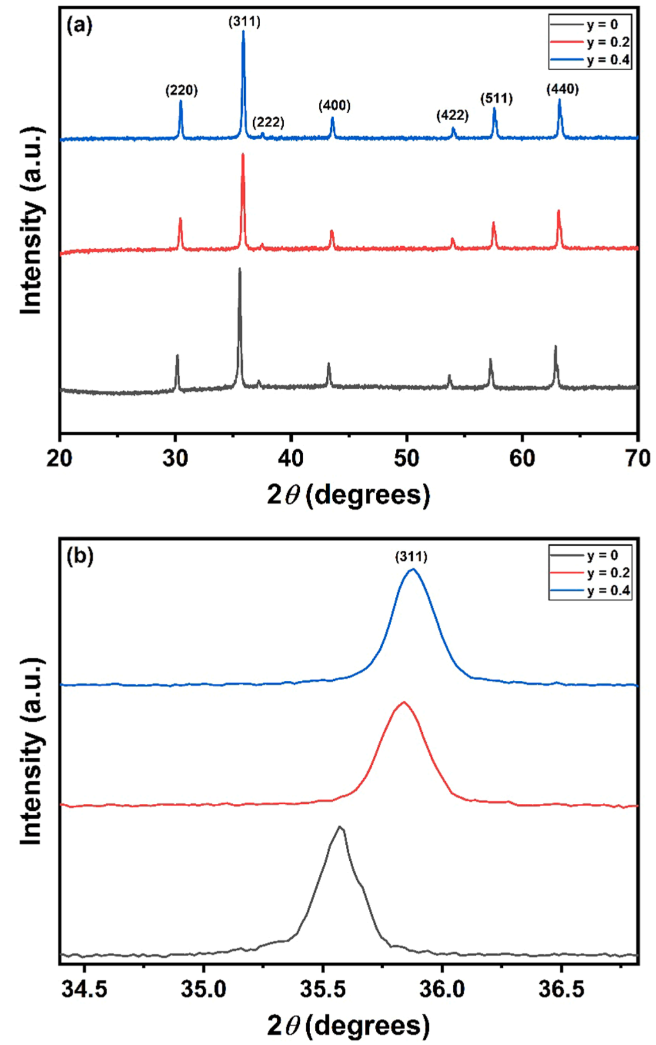

Fig. 1. (a) XRD patterns of LCCFO−0, LCCFO−0.2, and LCCFO−0.4 ferrites. (b) Magnified view of the most intense (311) peak from the corresponding XRD patterns.

Table 1
Structural parameters of LCCFO−0, LCCFO−0.2 and LCCFO−0.4 spinel ferrites. The crystallite size (*D*) values are reported with an estimated uncertainty of ±0.1 nm, derived from the variation in the FWHM used in the Debye–Scherrer calculation.

Sample name	*a* (Å)	*D* (nm)	d_{X-ray} (g/cm^3)	d_{ex} (g/cm^3)	*P*%	*S* (m^2/g)
LCCFO−0	8.361	37.1	5.17	4.64	10.2	34.85
LCCFO−0.2	8.310	35.4	5.26	4.56	13.3	37.17
LCCFO−0.4	8.302	37.2	5.25	4.75	9.5	33.95

parameter, as it strongly affects the interaction between water vapor and the sensing surface. Consequently, porous oxide-based materials have attracted considerable interest due to their ability to facilitate enhanced vapor adsorption and improved sensing performance.

A number of earlier investigations have underscored the suitability of spinel-type oxides for humidity detection. Rezlescu and co-workers [11] showed that Mg-based ferrites can display pronounced humidity sensitivity, with their response influenced by factors such as composition, crystallite dimensions, surface area, and porosity. Kassas et al. [12] examined porous Li–Mg–Ti–O–F ceramics and observed that their sensitivity remained relatively low below about 55% relative humidity (%RH). Kuang et al. [13] explored individual SnO_2 nanowires and reported favorable sensing features. Ferrite materials intended for humidity applications have been produced through several synthesis routes, including solid-state processing [14], chemical co-precipitation [15], and other thermal methods [16]. For example, Manikandan et al. [15] prepared lithium-substituted copper ferrite films via co-precipitation and obtained a moderate sensitivity of 2.2 MΩ/%RH. Likewise, Kotnala et al. [14] investigated lithium-modified magnesium ferrite fabricated by solid-state reaction and reported sensitivities ranging from 165 to 2080 within the 10–80% RH window. Patil et al. [17] reported cation distribution and magnetic properties in Cr-substituted lithium ferrite, while Patange et al. [18] investigated the electrical and magnetic properties of Cr^{3+}-substituted nanocrystalline nickel ferrite. Raju et al. [19] examined the effect of chromium substitution on the structural and magnetic properties of cobalt ferrite. To date, no studies have reported chromium substitution in the lithium–copper ferrite system for humidity sensing applications.

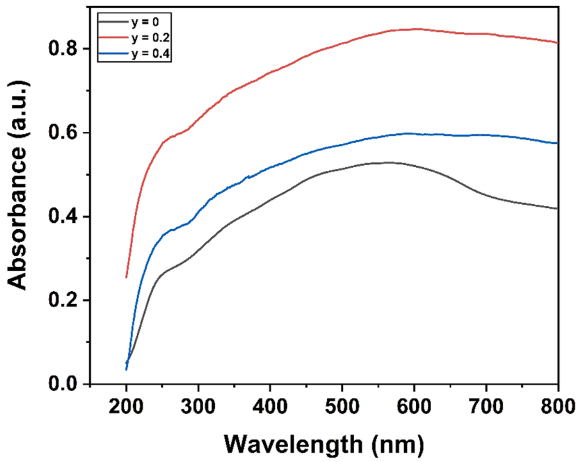

Fig. 2. UV–Vis absorption spectra of LCCFO−0, LCCFO−0.2, and LCCFO−0.4 ferrites.

Accordingly, the present study provides a comprehensive assessment of the humidity-sensing performance of chromium-substituted lithium–copper ferrites. The samples were subjected to precisely controlled humidity levels, generated through saturated salt solutions in a sealed chamber, enabling the determination of key sensing parameters such as sensitivity, response time, and recovery time.

The originality of the present work lies in the design and comprehensive evaluation of chromium-substituted lithium–copper ferrites ($Li_xCu_{1-x}Cr_yFe_{2-y}O_4$) as resistive humidity sensing materials, a composition that, to the best of our knowledge, has not been previously reported for this application. In contrast to earlier studies on Cr-doped single-cation ferrites (such as Li, Ni, or Co ferrites), a mixed Li–Cu spinel system is investigated, in which the Cr^{3+} content is systematically varied (y = 0, 0.2, 0.4) and correlated with structural parameters (lattice constant, crystallite size, porosity), optical band gap, and humidity sensing performance over a wide RH range. This study further distinguishes itself by combining detailed microstructural characterization with quantitative humidity response analysis—including sensitivity, response/recovery times, and long-term stability over 90 days—and by interpreting the sensing behavior through the Freundlich adsorption isotherm, providing deeper insight into the role of Cr-induced defects and surface active sites in governing protonic conduction in spinel ferrite-based humidity sensors.

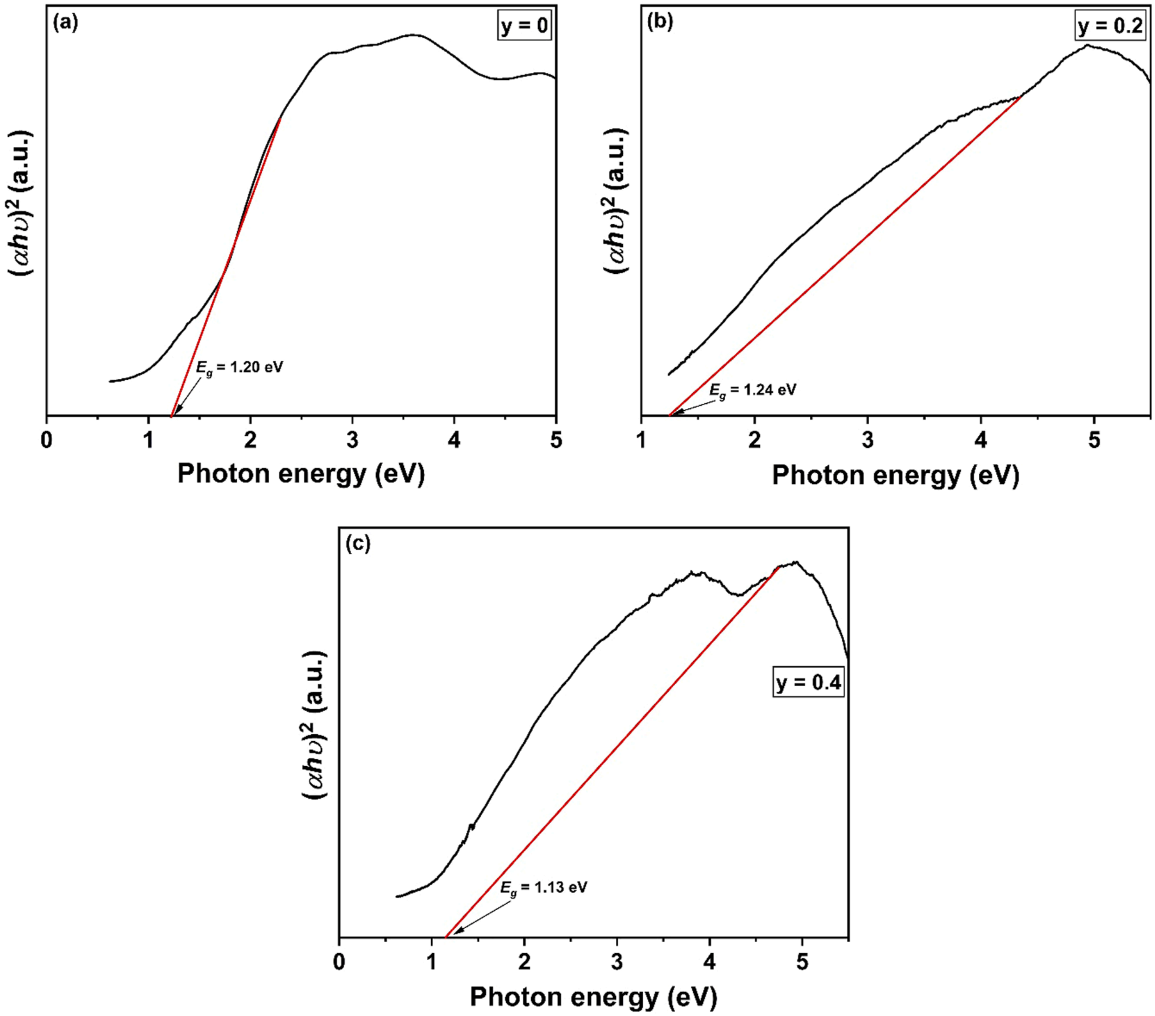

Fig. 3. Tauc plots of LCCFO−0, LCCFO−0.2, and LCCFO−0.4, used for the estimation of the optical band gap values.

2. Materials and methods

2.1. *Synthesis and characterization of ferrite materials*

Polycrystalline ferrites with the nominal composition $Li_xCu_{1-x}Cr_yFe_{2-y}O_4$ (x = 0.2; y = 0, 0.2, 0.4) were synthesized through a conventional ceramic route and are referred to as LCCFO−0, LCCFO−0.2, and LCCFO−0.4, respectively. Analytical-grade oxide precursors—Li_2O (99.5%, Thermo Fisher Scientific), CuO (99%, Alfa Aesar), Cr_2O_3 (99%, Alfa Aesar), and Fe_2O_3 (98%, Alfa Aesar)—were weighed in stoichiometric proportions using a single-pan balance.

The mixed oxides were wet milled in acetone for 3 h and subsequently pre-sintered at 700 °C for 24 h with a heating rate of 80 °C/h. The pre-sintered powders were then milled again under identical conditions and finally sintered at 1000 °C for 48 h. After sintering, the material was crushed to obtain fine powders.

For pellet preparation, a 5% polyvinyl alcohol (PVA) solution was incorporated as a binder. Pellets with a diameter of 10 mm and thickness between 1 and 1.5 mm were pressed under 10 tons and later sintered at 700 °C for 10 h (heating rate: 80 °C/h).

The structural properties of the synthesized ferrites were characterized by X-ray diffraction (XRD) using a Rigaku D/Max−2400 diffractometer with Cu-Kα radiation (λ = 1.5406 Å), operating at 40 kV and 30 mA, with a step interval of 0.02° over the 2θ range of 20–70°. Surface morphology and elemental composition were analyzed using a JEOL JSM−6360 scanning electron microscope (SEM) equipped with an energy-dispersive X-ray (EDX) system. Optical measurements were obtained using a Jasco V−770 ultraviolet–visible (UV–Vis) spectrophotometer, while Fourier transform infrared (FTIR) spectra were recorded using a Jasco FT/IR−6100 instrument to evaluate metal–oxygen vibrations and the presence of adsorbed water or atmospheric CO_2. Brunauer–Emmett–Teller (BET) analysis was performed on the ferrite samples using Quantachrome TouchWin v1.11 to determine the specific surface area and pore size distribution. X-ray photoelectron spectroscopy (XPS) was carried out using a Thermo Scientific K-Alpha system to investigate the chemical composition of the samples.

2.2. *Humidity sensing measurements*

Controlled humidity environments were generated using saturated aqueous solutions of NaOH, $CaCl_2 \cdot 6\ H_2O$, K_2CO_3, $Mg(NO_3)_2$, $NaNO_3$, NaCl, KCl, and K_2SO_4, producing relative humidity (RH) levels of 8.9, 31, 43, 52, 63, 75, 86, and 97%, respectively [20–24]. The RH values were confirmed using a calibrated hygrometer.

The direct current (DC) electrical resistance of the pelletized samples at different humidity levels was measured via the two-probe method. Conductive silver paste was applied to both pellet surfaces to ensure ohmic contact, and the samples were interfaced with a Keithley 2450 (6½-digit) source meter. All measurements were carried out at room temperature, with each sample allowed to equilibrate at the target RH until saturation. Response and recovery characteristics were evaluated over the full 8.9–97% RH range.

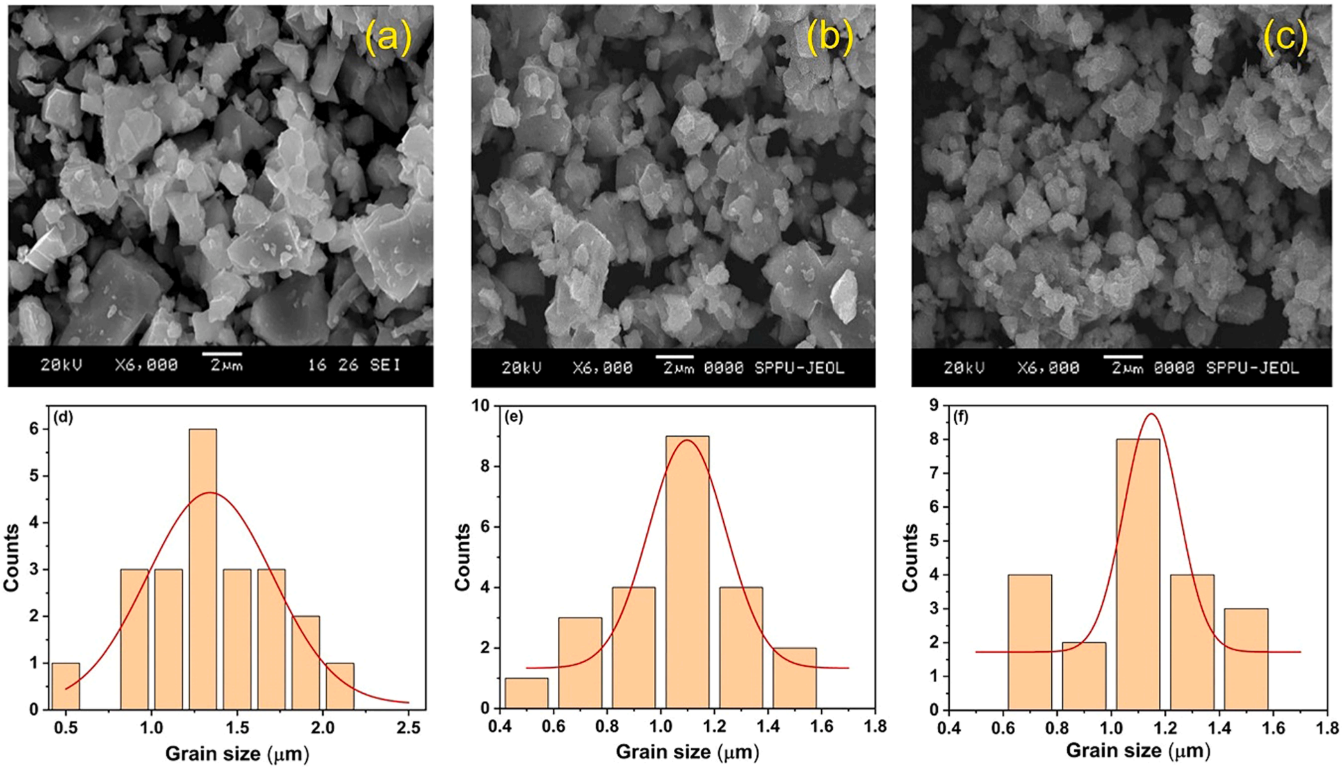

Fig. 4. SEM micrographs and corresponding grain size distributions of (a,d) LCCFO−0, (b,e) LCCFO−0.2, and (c,f) LCCFO−0.4 ferrites. The histograms with Gaussian fitting curves represent the grain size distribution obtained from ImageJ analysis.

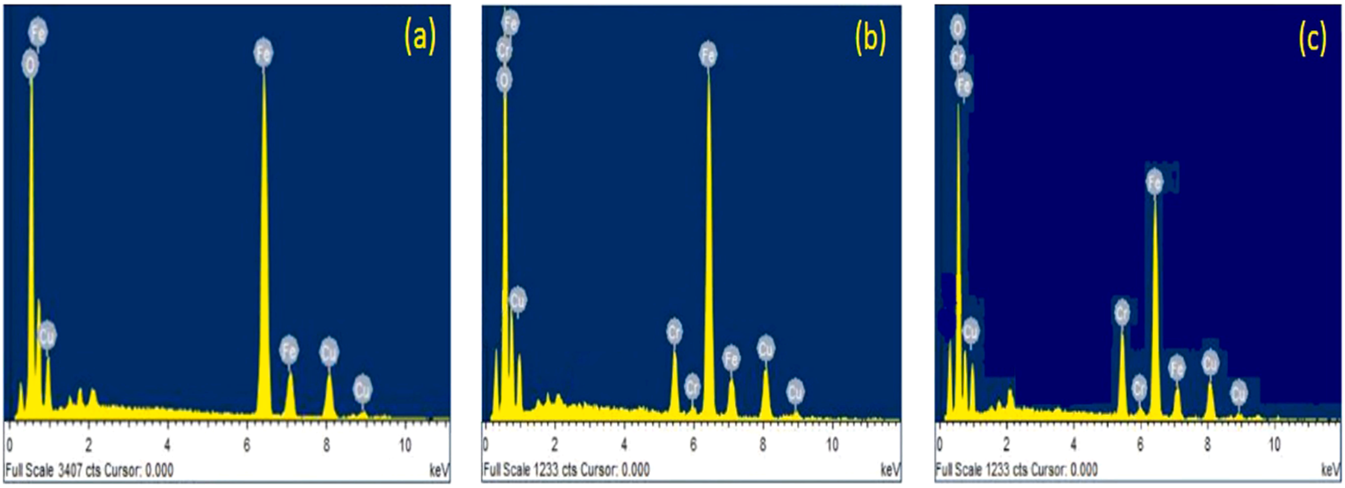

Fig. 5. EDX spectra of (a) LCCFO−0, (b) LCCFO−0.2, and (c) LCCFO−0.4 ferrites.

3. Results and discussion

3.1. X-ray diffraction

The structural characteristics of the LCCFO−0, LCCFO−0.2, and LCCFO−0.4 ferrites were examined by XRD. All compositions exhibited a single-phase cubic spinel structure belonging to the Fd3m space group. The diffraction patterns contained reflections corresponding to the (220), (311), (222), (400), (422), (511), and (440) planes (Fig. 1a), consistent with the Joint Committee on Powder Diffraction Standards (JCPDS) reference card no. 40–1120.

A progressive decrease in lattice constant was observed as the chromium content increased from y = 0 to y = 0.4 (Table 1). This contraction reflects the substitution of Fe^{3+} ions (0.67 Å) with the slightly smaller Cr^{3+} ions (0.64 Å). The shift of the (311) peak toward higher 2θ values further confirms the reduction in lattice parameter resulting from Cr incorporation (Fig. 1b). The Cr^{3+} ions exhibit a strong preference for octahedral sites in the spinel lattice [17,18,25,26]. Crystallite sizes (D), determined using the Debye–Scherrer equation,

$$D = \frac{0.9\ \lambda}{\beta\ \cos\theta} \tag{1}$$

were found to lie between 37.1 and 37.2 nm, as summarized in Table 1. Here, $\lambda = 1.5406$ Å corresponds to the Cu-Kα radiation, β is the full width at half maximum (FWHM) of the principal diffraction peak (in radians), and θ is the associated Bragg angle.

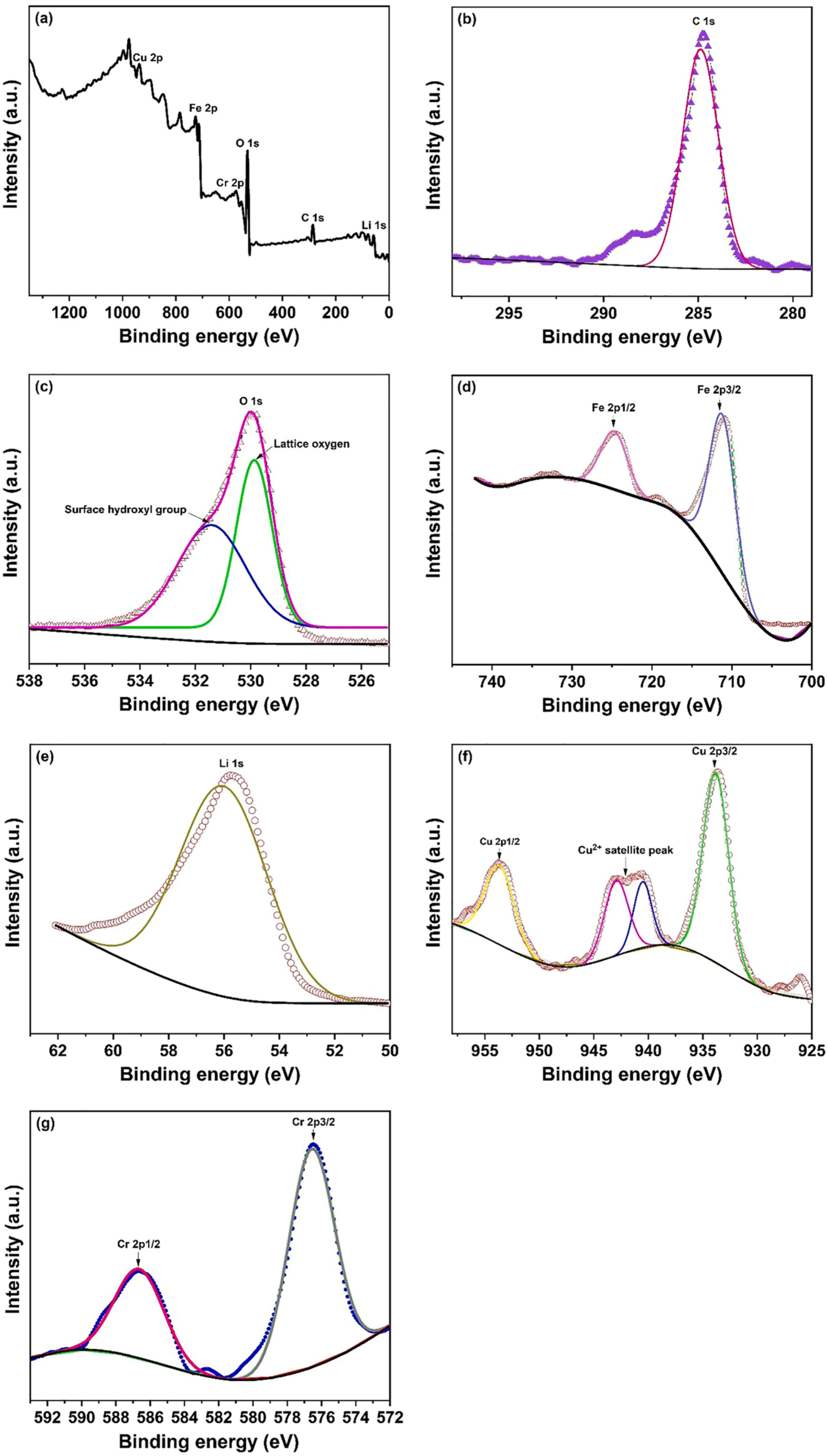

Fig. 6. XPS spectra of LCCFO−0.2: (a) survey spectrum and high-resolution spectra of (b) C 1s, (c) O 1s, (d) Fe 2p, (e) Li 1s, (f) Cu 2p, and (g) Cr 2p.

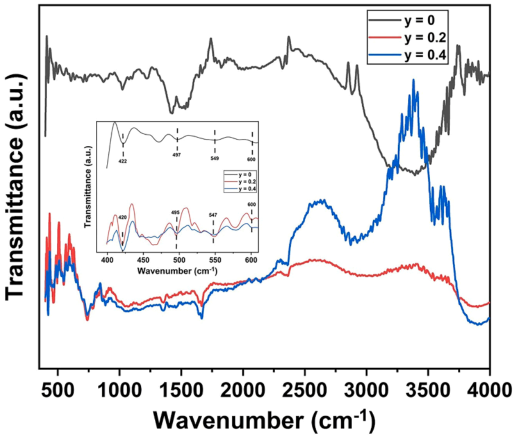

Fig. 7. FTIR spectra of LCCFO−0, LCCFO−0.2 and LCCFO−0.4 ferrites. Inset: enlarged view of the 385–610 cm^{-1} region.

The theoretical X-ray density was calculated using:

$$d_{X-ray} = \frac{8\ M}{N\ a^3} \tag{2}$$

where M denotes the molecular weight of the composition, N is Avogadro's number, and a is the lattice constant. The experimental density was obtained from the mass-to-volume ratio:

$$d_{ex} = \frac{\text{Mass of the sample}}{\text{Volume of the sample}} \tag{3}$$

Porosity (P%) was then estimated through the relation:

$$P\% = \left(\frac{d_{X-ray}\ -\ d_{ex}}{d_{X-ray}}\right) \times 100 \tag{4}$$

where d_{X-ray} and d_{ex} correspond to the theoretical and experimental densities, respectively.

Finally, the specific surface area (S) was estimated using the relation:

$$S = \frac{6000}{D\,d_{ex}} \tag{5}$$

As shown in Table 1, the difference between the X-ray and experimental densities confirms the presence of porosity in the samples [27]. The bulk density first decreases and then increases with chromium content, resulting in a corresponding increase and subsequent decrease in porosity, consistent with the inverse relationship between bulk density and porosity [28]. The reduction in porosity at higher Cr content may be associated with enhanced densification during sintering. The specific surface area increases with chromium substitution due to the reduction in crystallite size. Smaller crystallite sizes provide a larger number of surface atoms, thereby increasing the available surface area [29,30].

3.2. UV–Visible spectroscopy

The UV–Vis absorption spectra of the chromium-substituted lith-

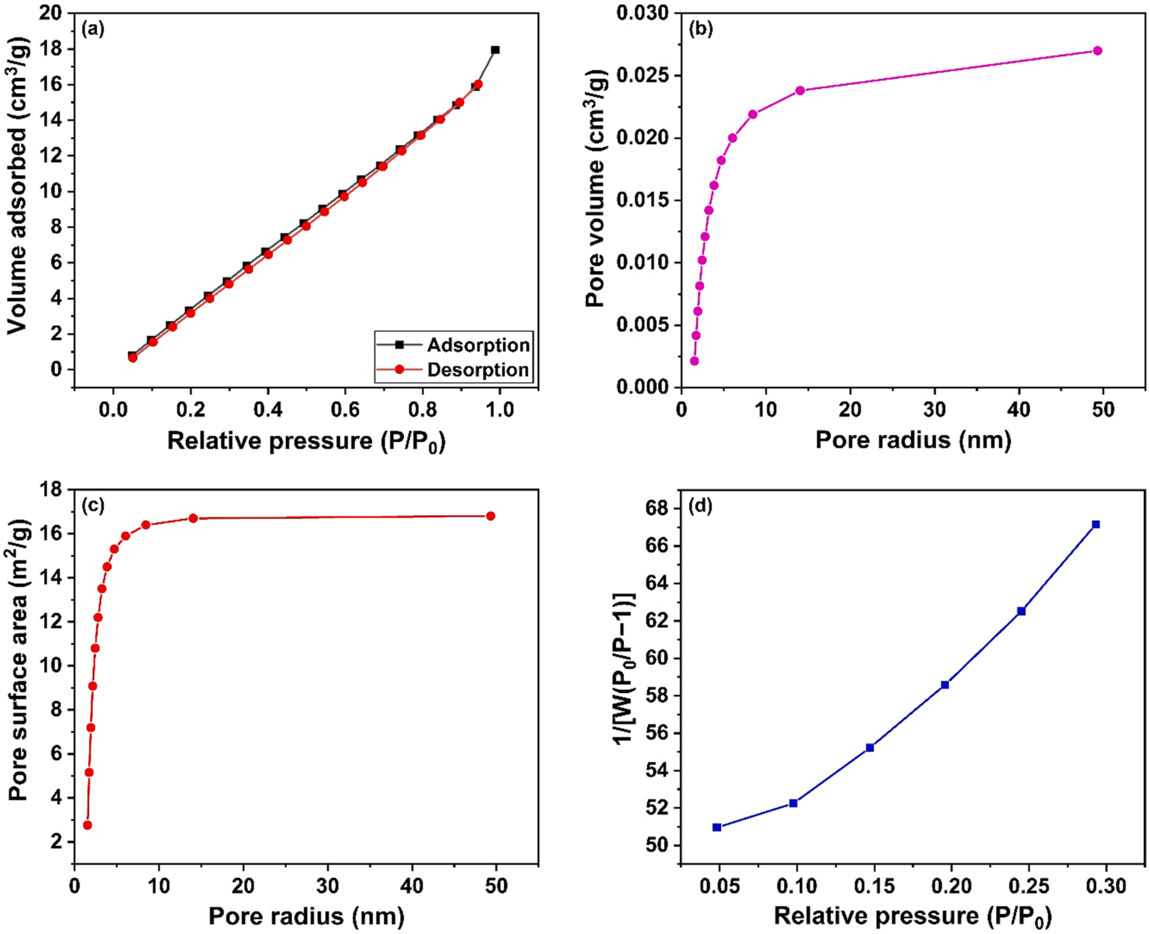

Fig. 8. BET analysis of LCCFO−0.2: (a) nitrogen adsorption–desorption isotherm, (b) pore volume *vs.* pore radius distribution, (c) pore surface area *vs.* pore radius, and (d) BET linear plot.

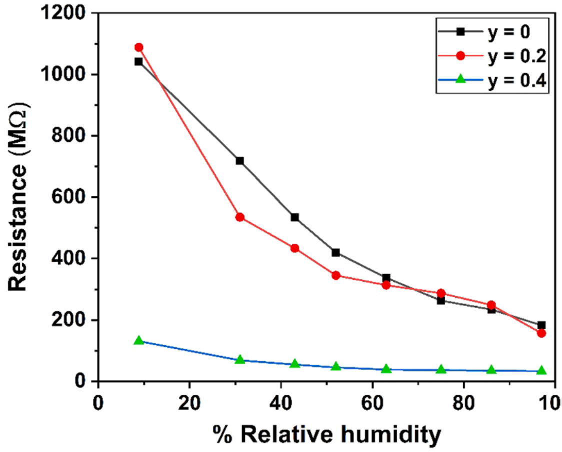

Fig. 9. Variation of electrical resistance with relative humidity for LCCFO−0, LCCFO−0.2, and LCCFO−0.4 samples.

ium–copper ferrites are presented in Fig. 2. The optical band gap (E_g) of the LCCFO−0, LCCFO−0.2, and LCCFO−0.4 samples was extracted using Tauc analysis, based on the absorbance–wavelength data obtained from the spectrophotometer. More in detail, band gap estimation was performed by plotting $(\alpha h\nu)^2$ as a function of photon energy ($h\nu$) and extrapolating the linear portion of the curve to the energy axis, as illustrated in Fig. 3. The relation employed for this purpose is:

$$(\alpha h\nu)^2 = A(h\nu - E_g) \quad (6)$$

where α denotes the absorption coefficient, h is Planck's constant, ν represents the photon frequency, and A is a proportionality constant.

The resulting band gaps were found to be 1.20 eV for LCCFO−0, 1.24 eV for LCCFO−0.2, and 1.13 eV for LCCFO−0.4. The moderate widening of the gap at $y = 0.2$ is attributed to the introduction of additional charge carriers associated with chromium substitution, consistent with the preferential occupation of Fe^{3+} sites by Cr^{3+} ions in the spinel lattice. This behavior can be explained by a Burstein–Moss-type effect [31,32], in which the population of states near the conduction band leads to a shift of the Fermi level toward higher energies [33,34]. At higher Cr content ($y = 0.4$), the decrease in band gap is likely linked to the formation of oxygen vacancies at grain or particle interfaces, which introduce localized states within the band structure and increase structural disorder, thereby reducing the effective band gap [35–38]. All synthesized ferrites exhibit semiconducting characteristics.

3.3. Surface morphology

The surface features of the synthesized materials were examined using SEM, as illustrated in Fig. 4a–c. The micrographs display aggregates composed of irregularly shaped, cube-like particles with somewhat indistinct boundaries. A broad distribution of grain sizes is evident, a characteristic often favorable for humidity sensing. Such heterogeneous microstructures typically contain interconnected pores and void networks that promote water vapor penetration and, consequently, improve sensing performance.

Quantitative grain size analysis was carried out on the SEM micrographs using ImageJ software (Fig. 4d–f). The average grain size of the LCCFO−0 sample was found to be approximately 1.36 μm, while the Cr-substituted samples LCCFO−0.2 and LCCFO−0.4 exhibited smaller average grain sizes of about 1.06 μm and 1.08 μm, respectively. This trend is consistent with the observed microstructure, indicating that chromium substitution induces a moderate grain refinement without significantly altering the overall morphology. The reduction in grain size, together with the increased porosity and specific surface area—particularly for LCCFO−0.2—suggests a higher density of surface active sites, which can enhance water vapor adsorption and diffusion, thereby contributing to the improved humidity sensing performance.

Elemental composition was assessed through EDX analysis (Fig. 5a–c). For the LCCFO−0 sample, the spectra indicate the presence of copper, iron, and oxygen, whereas the LCCFO−0.2 and LCCFO−0.4 samples additionally exhibit clear chromium signals. These results confirm the successful incorporation of Cr ions into the $Li_{0.2}Cu_{0.8}Fe_{1.8}O_4$ lattice.

3.4. X-ray photoelectron spectroscopy

XPS was employed to investigate the elemental composition and chemical states of the chromium-substituted lithium–copper ferrite. Fig. 6a–g presents the survey and high-resolution spectra for the representative LCCFO−0.2 sample. The survey spectrum (Fig. 6a) confirms the presence of all constituent elements (C, O, Fe, Li, Cu, and Cr), indicating successful incorporation of chromium into the ferrite lattice. The high-resolution C 1s spectrum (Fig. 6b) shows a main peak at

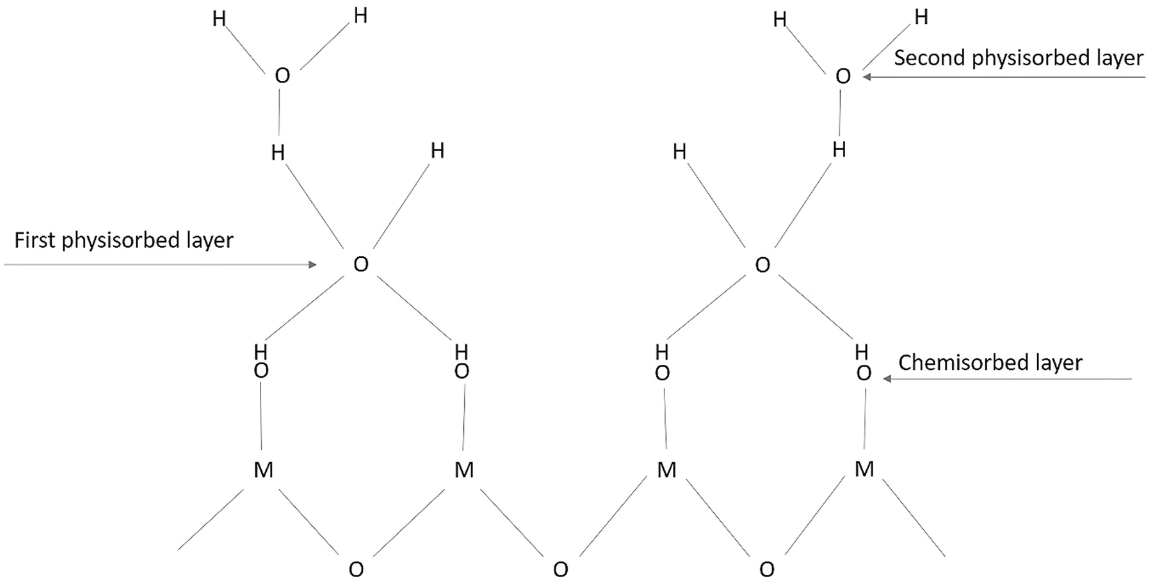

Fig. 10. Schematic representation of the Grotthuss proton-hopping mechanism responsible for charge transport at high humidity levels.

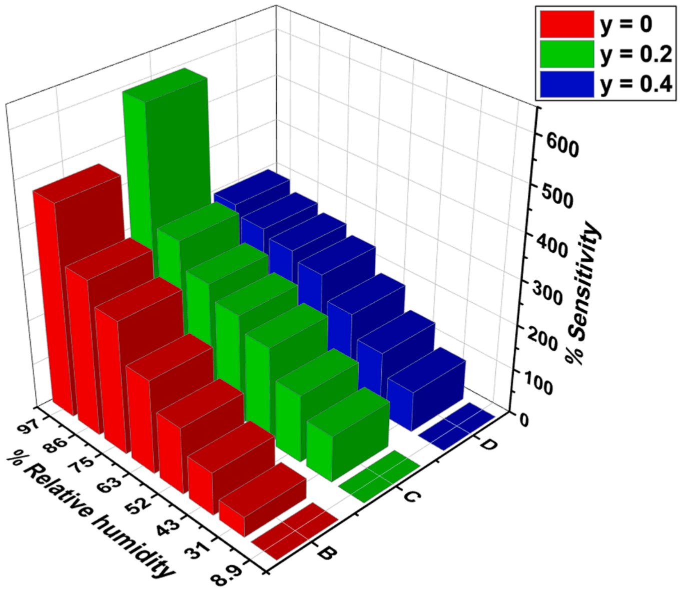

Fig. 11. Humidity sensitivity of LCCFO−0, LCCFO−0.2, and LCCFO−0.4 as a function of relative humidity.

Table 2
Comparative sensitivity of LCCFO−0.2 with other ferrite-based humidity sensors.

Ferrite compound	Sensitivity	Reference
Li-$CuFe_2O_4$	2.2 MΩ/%RH	[15]
$MgFe_2O_4$	(230 ± 11) %	[20]
$NiFe_2O_4$	(249 ± 20) %	[20]
$CuFe_2O_4$	(267 ± 8) %	[20]
$CoFe_2O_4$	590%	[24]
LCCFO−0.2	595%	Present study

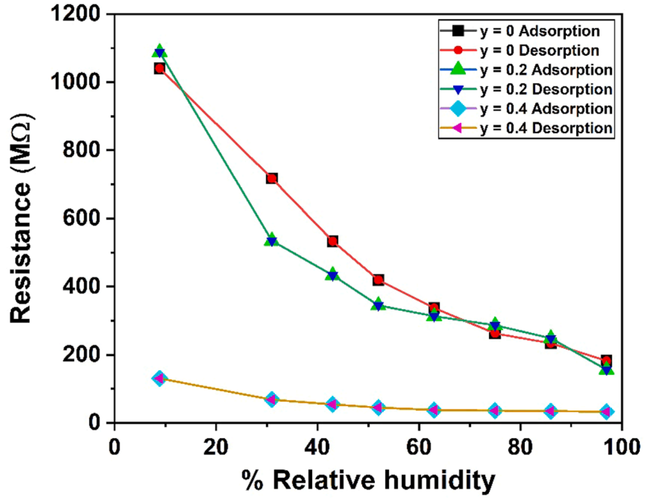

Fig. 12. Hysteresis curves of LCCFO−0, LCCFO−0.2 and LCCFO−0.4 ferrites.

~284.87 eV, attributed to adventitious carbon species. The O 1s spectrum (Fig. 6c) exhibits two components: the peak at ~529.87 eV corresponds to lattice oxygen, while the peak at ~531.43 eV is associated with surface hydroxyl groups [39,40], indicating the presence of surface-active sites. The Fe 2p spectrum (Fig. 6d) shows characteristic peaks at ~711.19 eV (Fe 2p3/2) and ~724.75 eV (Fe 2p1/2), confirming the presence of Fe^{3+} ions in the spinel structure [41,42]. The Li 1s peak (Fig. 6e) is observed at ~56.02 eV, consistent with lithium incorporation [43]. The Cu 2p spectrum (Fig. 6f) displays peaks at ~933.80 eV (Cu 2p3/2) and ~953.76 eV (Cu 2p1/2), along with a satellite feature at ~941.91 eV, characteristic of Cu^{2+} species [44,45]. The Cr 2p spectrum (Fig. 6g) shows peaks at ~576.52 eV (Cr 2p3/2) and ~586.72 eV (Cr 2p1/2), confirming the presence of Cr^{3+} ions in the spinel lattice [46]. Overall, the XPS analysis confirms the successful incorporation of chromium and supports the modification of the electronic structure and defect chemistry discussed in the previous sections.

3.5. *FTIR analysis*

The FTIR spectra of the sintered LCCFO−0, LCCFO−0.2, and LCCFO−0.4 samples, recorded over the 400–4000 cm^{-1} range, are shown in Fig. 7. The most prominent features appear in two regions: 420–497 cm^{-1} and 547–600 cm^{-1}. These bands correspond to metal–oxygen stretching vibrations associated with octahedral and tetrahedral coordination sites, respectively. Shifts in the positions of these bands reflect variations in Fe–O bond lengths within the spinel lattice, a behavior commonly observed in ferrite systems [47].

Additional spectral features occur at higher wavenumbers. A peak near 2360 cm^{-1} is attributed to C=O stretching from ambient CO_2 [48], while the band around 1630 cm^{-1} arises from O–H bending vibrations of adsorbed water molecules [48]. A broad absorption near 3500 cm^{-1} is also present, which corresponds to H–O–H stretching and bending modes associated with physisorbed or weakly bound water [49].

3.6. *BET analysis*

BET analysis was performed to evaluate the specific surface area and pore characteristics of $Li_xCu_{1-x}Cr_yFe_{2-y}O_4$ (x = 0.2, y = 0.2). Nitrogen adsorption–desorption measurements were carried out at 77 K, and the corresponding results are shown in Fig. 8a–d for the representative LCCFO−0.2 sample. The adsorption–desorption isotherm (Fig. 8a) exhibits a type-IV profile, indicative of a mesoporous structure. The pore size distribution (Fig. 8b) confirms the presence of mesopores, with an average pore radius of approximately 7.86 nm. The variation of pore surface area with pore radius (Fig. 8c) further supports the dominant contribution of mesoporous features. The BET linear plot (Fig. 8d) was used to determine the specific surface area, which was found to be 30.72 m^2/g. The corresponding pore volume was estimated to be 0.0142 cm^3/g. These results indicate that LCCFO−0.2 possesses a well-developed mesoporous structure, which is expected to enhance water vapor adsorption and facilitate charge transport during humidity sensing.

3.7. *Humidity sensing response*

In this study, the humidity-sensing behavior of $Li_xCu_{1-x}Cr_yFe_{2-y}O_4$ (x = 0.2; y = 0, 0.2, 0.4) was examined over a relative humidity range of 8.9–97% RH. Fig. 9 illustrates the change in electrical resistance as a function of humidity for all compositions. A clear trend is observed in which the resistance decreases progressively with increasing RH.

At low humidity levels (8.9–31% RH), the initial drop in resistance is attributed to chemisorption. In this regime, a primary layer of hydroxyl species forms as water molecules dissociate on the ferrite surface, generating protons and hydroxyl ions ($H_2O \rightarrow H^+ + OH^-$). The hydroxyl groups bind to cationic sites, while the increased surface energy of the crystallites favors dissociative adsorption [50–53].

In the intermediate humidity region (31–63% RH), the adsorbed protons interact with additional water molecules to produce hydronium ions ($H^+ + H_2O \rightarrow H_3O^+$). As humidity rises further, physisorbed water layers build upon the initial chemisorbed layer, increasing the number of mobile charge carriers and producing a corresponding decrease in resistance.

At high humidity (63–97% RH), multiple physisorbed layers

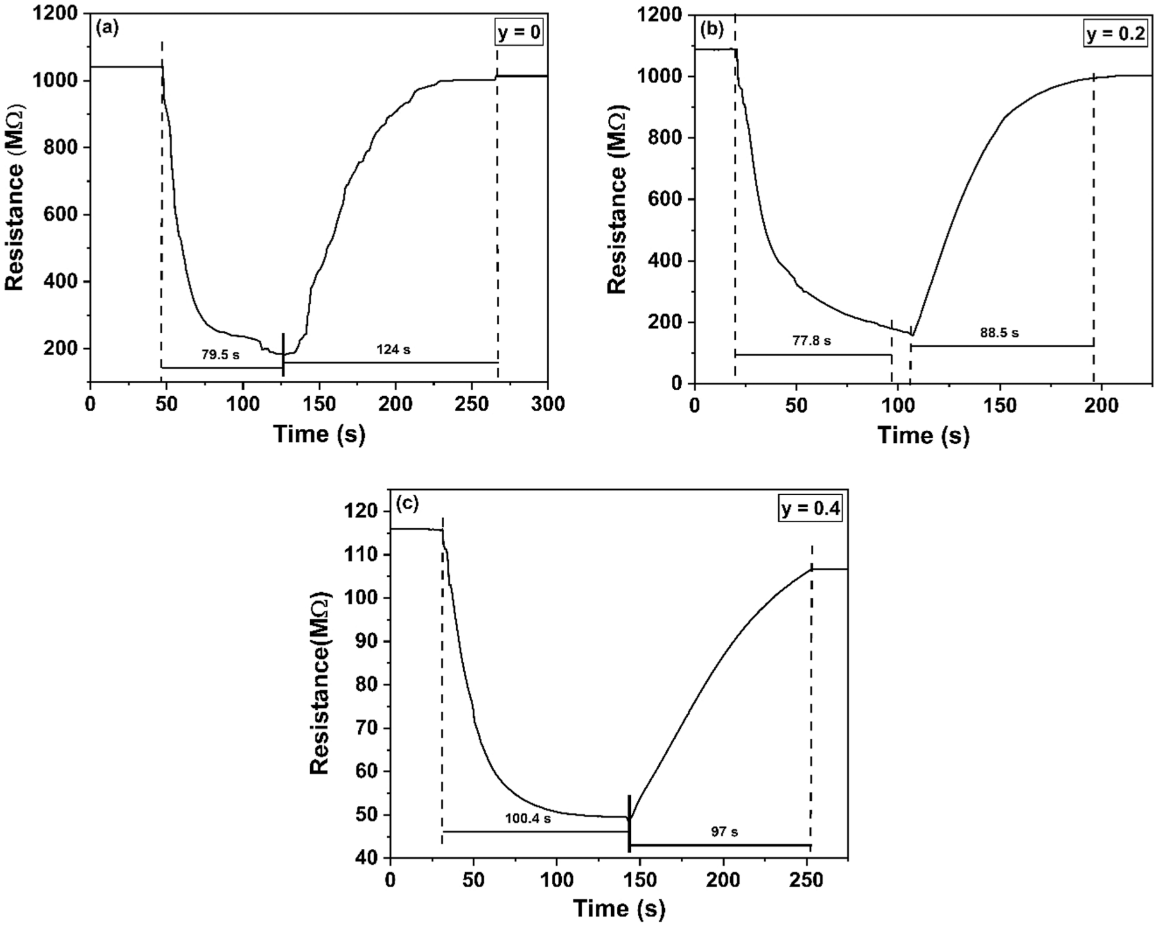

Fig. 13. Response and recovery times of (a) LCCFO−0, (b) LCCFO−0.2, and (c) LCCFO−0.4 sensors under humidity cycling between 8.9% RH and 97% RH.

accumulate and capillary condensation becomes significant. Under these conditions, hydronium ions may undergo dissociation ($H_3O^+ \rightarrow H^+ + H_2O$), releasing protons that transfer between adjacent water molecules. This proton-hopping process, commonly referred to as the Grotthuss mechanism [54], provides an efficient pathway for charge transport and results in a more pronounced resistance drop. A schematic representation of this mechanism is shown on Fig. 10.

Sensitivity is a key figure of merit for any humidity sensor, since dependable performance requires a pronounced and measurable response across the full range of operating conditions. The sensitivity S (%) of the LCCFO−0, LCCFO−0.2, and LCCFO−0.4 samples was determined using the expression:

$$S\,(\%) = \frac{R_{8.9} \; - \; R_x}{R_x} \times 100 \tag{7}$$

where $R_{8.9}$ denotes the resistance measured at the lowest relative humidity (8.9% RH), and R_x corresponds to the resistance recorded at a given humidity level [23,55,56].

Fig. 11 shows the sensitivity of LCCFO−0, LCCFO−0.2, and LCCFO−0.4 as a function of relative humidity. Among the three compositions, LCCFO−0.2 demonstrates the strongest response, reaching a maximum sensitivity of 595%. This improvement is closely linked to its microstructural characteristics, particularly its porosity and crystallite dimensions. Higher porosity increases the number of accessible adsorption sites for water molecules, promoting more efficient vapor diffusion and enhancing the overall sensing response. Likewise, smaller crystallite size contributes additional surface-active regions that support adsorption–desorption processes.

To contextualize its performance, the sensitivity of LCCFO−0.2 was compared with previously reported values for ferrite-based humidity sensors. A summary of this comparison is provided in Table 2.

The hysteresis behavior of the sensing elements was evaluated by first increasing the relative humidity from 8.9% to 97% RH and then reducing it back to 8.9% RH, while recording the resistance at each step. Hysteresis reflects the difference between adsorption and desorption pathways during humidity cycling. Fig. 12 shows the hysteresis curves obtained for the LCCFO−0, LCCFO−0.2, and LCCFO−0.4 samples.

The hysteresis error (H_e) was calculated using the relation:

$$H_e = \pm \frac{\Delta R_{\max}}{2 \; F_{FS}} \tag{8}$$

where $\Delta R_{\max}$ represents the maximum deviation between the adsorption and desorption branches, and F_{FS} denotes the full-scale output [23,57,58]. This parameter provides insight into the reliability and stability of the sensing response. The hysteresis curves indicate that the adsorption and desorption paths nearly overlap for all samples. The maximum H_e for LCCFO−0 was observed at 86% RH with a value of 1.04%, while LCCFO−0.2 exhibited a lower value of 0.53% at 63% RH. For LCCFO−0.4, the maximum H_e reached 1.33% at 31% RH. The relatively low H_e values ($\leq$ 1–1.3%) indicate good reliability and repeatability of the sensing behavior [39].

The response and recovery times provide insight into how quickly a sensor can react to changes in ambient humidity. In this work, the response time was defined as the interval required for the resistance to reach 90% of its total change when the humidity was increased from 8.9% to 97% RH. Conversely, the recovery time corresponds to the period needed for the resistance to return to 90% of its initial value when the humidity was reduced from 97% RH back to 8.9% RH. Fig. 13

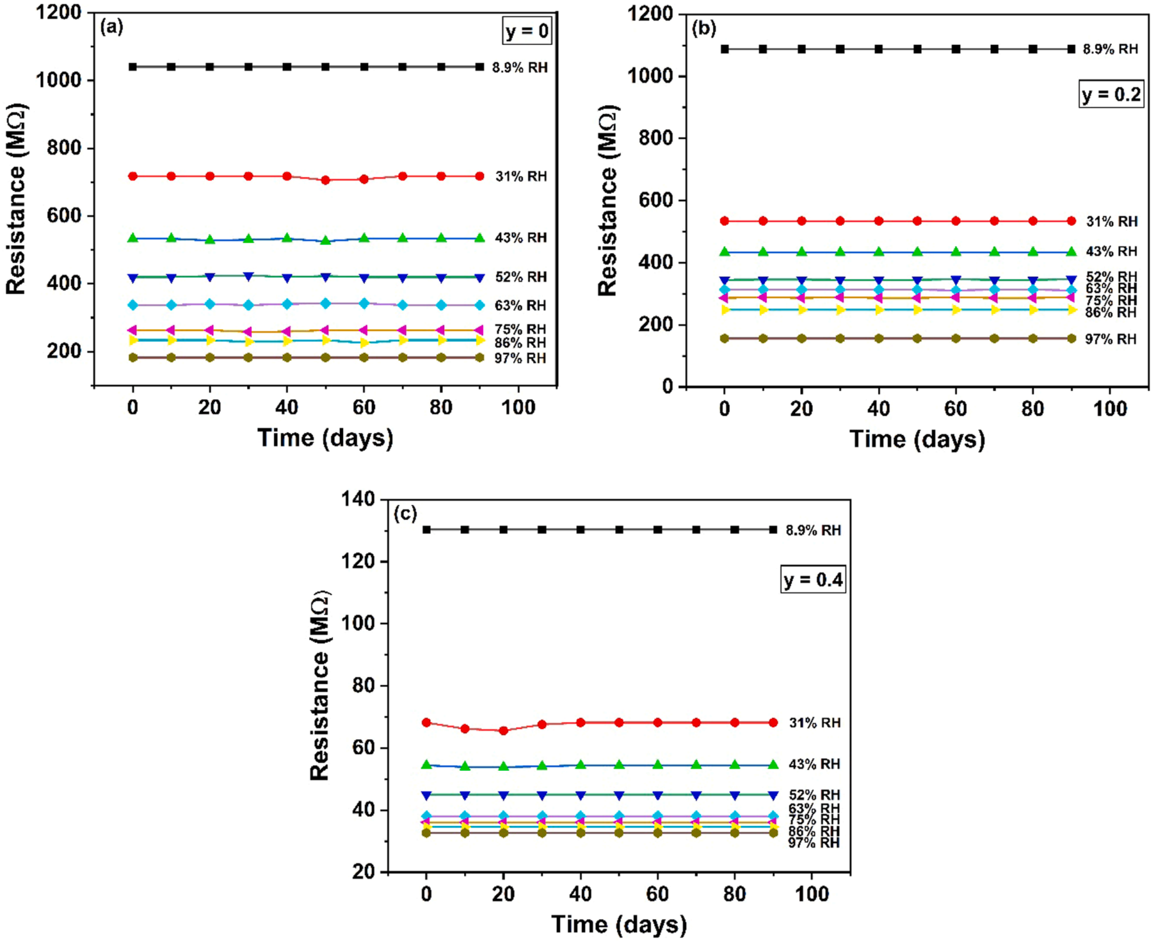

Fig. 14. Long-term stability of (a) LCCFO−0, (b) LCCFO−0.2, and (c) LCCFO−0.4 sensors monitored over 90 days under different humidity conditions.

presents the response and recovery characteristics of the LCCFO−0, LCCFO−0.2, and LCCFO−0.4 samples.

Among the compositions, LCCFO−0.2 exhibited the fastest dynamics, with response and recovery times of 77.8 s and 88.5 s, respectively, during a full adsorption–desorption cycle. This improved performance is attributed to its higher concentration of open and interconnected pores, which accelerates water vapor diffusion throughout the material.

Stability is another important criterion for evaluating long-term sensor performance [59,60]. To assess this property, the resistance of each sample was recorded at various humidity levels over a 90-day period, with measurements taken every 10 days. The long-term stability profiles of LCCFO−0, LCCFO−0.2, and LCCFO−0.4 are shown in Fig. 14.

3.8. *Relative deviation in resistance and Freundlich adsorption isotherm model*

The relative deviation in resistance (ΔR_H) provides a quantitative measure of the sensor response under varying humidity conditions and is particularly relevant for evaluating device performance during transitions between different RH environments. Fig. 15a shows the variation of ΔR_H as a function of relative humidity for all compositions, revealing the presence of two distinct regions. This behavior is associated with the underlying conduction mechanism, where the region before and after the transition point (T_c) corresponds to conduction dominated by chemisorbed and physisorbed water layers, respectively. The different slopes observed in the ranges 8.9–52% RH and 52–97% RH further support the existence of two conduction regimes.

The relative deviation in resistance was calculated using the relation:

$$\%\Delta R_H = \frac{R_{LH} \; - \; R_H}{R_{LH}} \times 100 \tag{9}$$

where R_{LH} is the resistance measured at the lowest humidity level (8.9% RH), and R_H is the resistance at a given humidity.

When the sensor is exposed to a wide humidity range, a new adsorption–desorption equilibrium is established. This behavior can be attributed to van der Waals interactions and hydrogen bonding between adsorbed water molecules and surface active sites [23,61]. Ferrite materials are known to possess a large number of adsorption sites in the form of multi-cation centers; therefore, the Freundlich adsorption isotherm is appropriate for describing the surface adsorption mechanism in humidity sensors. The relationship between ΔR_H (representing the sensor response) and the relative humidity C (related to water vapor concentration) can be expressed as:

$$\Delta R_H = kC^{\alpha} \tag{10}$$

where k and α are constants representing the adsorption capacity and adsorption strength, respectively [61–63].

Fig. 15b presents the log–log plots of ΔR_H *vs.* relative humidity for LCCFO−0, LCCFO−0.2, and LCCFO−0.4, together with the corresponding Freundlich fits. Two linear regions are clearly observed, corresponding to low (8.9–52% RH) and high (52–97% RH) humidity ranges. The transition humidity (T_c) was determined from the intersection of the two linear fits. The T_c values were found to be 45.70%, 42.65%, and 44.15% for LCCFO−0, LCCFO−0.2, and LCCFO−0.4, respectively. The lower T_c observed for LCCFO−0.2 indicates an earlier

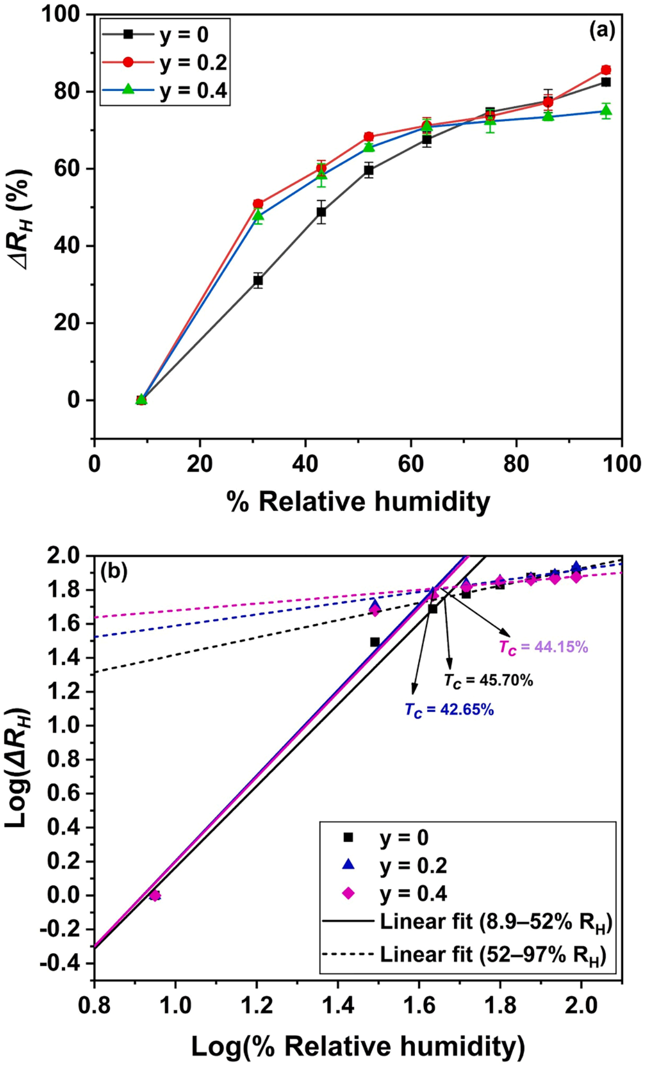

Fig. 15. (a) Relative deviation in resistance (ΔR_H) as a function of relative humidity for LCCFO−0, LCCFO−0.2, and LCCFO−0.4 samples. (b) Log–log plots of ΔR_H *vs.* relative humidity, showing the linear fitting of the Freundlich adsorption model in the low (8.9–52% RH) and high (52–97% RH) humidity regions, along with the corresponding transition humidity (T_c) values.

Table 3
Freundlich adsorption parameters for LCCFO−0, LCCFO−0.2 and LCCFO−0.4 in the low (8.9–52% RH) and high (52–97% RH) humidity regions. The constants k and α represent the adsorption capacity and adsorption strength, respectively, while R^2 denotes the goodness of fit of the linear regression.

Sample name	RH range (%)	k	α	R^2
LCCFO−0	8.9–52	1.24 ± 0.32	2.39 ± 0.22	0.98
	52–97	6.86 ± 0.07	0.50 ± 0.04	0.98
LCCFO−0.2	8.9–52	1.81 ± 0.57	2.52 ± 0.38	0.96
	52–97	13.61 ± 0.12	0.33 ± 0.06	0.93
LCCFO−0.4	8.9–52	1.77 ± 0.54	2.49 ± 0.37	0.96
	52–97	12.11 ± 0.06	0.20 ± 0.03	0.91

onset of physisorption-dominated conduction, which is beneficial for humidity sensing performance.

The Freundlich parameters k and α obtained for both regions are summarized in Table 3. The values of α are greater than unity in the low humidity region, indicating strong adsorption due to chemisorbed water layers. In contrast, α decreases significantly in the high humidity region, reflecting weaker adsorption associated with physisorbed multilayers. The overall trend of the parameters suggests that chromium substitution enhances the density of surface active sites, particularly for LCCFO−0.2, leading to improved adsorption behavior.

The Freundlich model thus provides a consistent interpretation of the sensing mechanism. At low humidity levels, charge transport is primarily governed by electronic conduction, as protons remain localized within chemisorbed and initial physisorbed layers. At higher humidity levels, the formation of continuous physisorbed water layers enables proton transport via the Grotthuss mechanism, leading to dominant protonic conduction and a significant decrease in resistance. Additionally, previously adsorbed and ionized oxygen species may influence the adsorption–desorption processes occurring at the sensor surface.

4. Conclusions

Polycrystalline $Li_xCu_{1-x}Cr_yFe_{2-y}O_4$ ferrites (x = 0.2; y = 0, 0.2, 0.4) were successfully prepared through a conventional ceramic synthesis route. XRD analysis verified the formation of a cubic spinel structure with nanometer-scale crystallite sizes, while SEM observations revealed a mixture of grain morphologies and a porous microstructure that is advantageous for humidity sensing. FTIR spectra showed the characteristic vibrational modes of ferrites, and UV–Vis measurements indicated that chromium substitution influences the optical band gap, producing a slight increase at y = 0.2 followed by a reduction at y = 0.4. XPS analysis confirmed the incorporation of Cr^{3+} ions and provided insight into the chemical states and defect structure, while BET measurements revealed a mesoporous structure with enhanced specific surface area.

Humidity-sensing tests carried out between 8.9% and 97% RH at room temperature confirmed that all samples displayed a decrease in resistance with increasing humidity. Among the investigated compositions, LCCFO−0.2 demonstrated the most promising performance, offering rapid response and recovery times (77.8 s and 88.5 s), high sensitivity (595% at 97% RH), and stable operation over a 90-day monitoring period. These advantages are attributed to its enhanced porosity and microstructural features that promote efficient water vapor adsorption and transport.

To further elucidate the adsorption–desorption processes occurring at the sensor surface, the experimental data were analyzed using the Freundlich adsorption isotherm model. The results provide additional insight into the role of surface active sites and confirm the suitability of LCCFO−0.2 as a reliable humidity-sensing material capable of operating effectively over a wide relative humidity range.

CRediT authorship contribution statement

Tripti Mandal: Conceptualization, Data curation, Investigation, Methodology, Writing – original draft. **Yesappa D. Kolekar:** Conceptualization, Funding acquisition, Investigation, Methodology, Supervision, Validation, Visualization. **Rakesh A. Afre:** Conceptualization, Formal analysis, Supervision, Validation, Writing – review & editing. **Diego Pugliese:** Conceptualization, Supervision, Visualization, Writing – review & editing. **Kishor M. Sonawane:** Conceptualization, Funding acquisition, Investigation, Methodology, Supervision, Validation, Visualization, Writing – review & editing.

Funding

This research did not receive any specific grant from funding agencies in the public, commercial, or non-profit sectors.

Declaration of Competing Interest

The authors declare that they have no known competing financial interests or personal relationships that could have appeared to influence the work reported in this paper.

Acknowledgements

Tripti Mandal and Kishor M. Sonawane gratefully acknowledge the Principal of Fergusson College, Pune, for granting permission to conduct this research work at the Department of Physics, Fergusson College (Autonomous), Pune. Diego Pugliese acknowledges the support from the European Union—NextGenerationEU under the National Recovery and Resilience Plan (NRRP), Mission 04 Component 2 Investment 3.1|Project Code: IR0000027—CUP: B33C22000710006—iENTRANCE@ENL: Infrastructure for Energy TRAnsition aNd Circular Economy @EuroNanoLab.

Data availability

Data will be made available on request.

References

[1] Z. Chen, C. Lu, Humidity sensors: a review of materials and mechanisms, Sens. Lett. 3 (2005) 274–295, https://doi.org/10.1166/sl.2005.045.

[2] U. Kang, K.D. Wise, A high-speed capacitive humidity sensor with on-chip thermal reset, IEEE Trans. Electron. Devices 47 (2000) 702–710, https://doi.org/10.1109/16.830983.

[3] P.-G. Su, C.-S. Wang, Novel flexible resistive-type humidity sensor, Sens. Actuators B Chem. 123 (2007) 1071–1076, https://doi.org/10.1016/j.snb.2006.11.015.

[4] F.-F. Chou, H.-W. Chang, T.-L. Li, J.-S. Shih, Piezoelectric crystal/surface acoustic wave biosensors based on fullerene C60 and enzymes/antibodies/proteins, J. Iran. Chem. Soc. 5 (2008) 1–15, https://doi.org/10.1007/BF03245810.

[5] A. Kharaz, B.E. Jones, A distributed optical-fibre sensing system for multi-point humidity measurement, Sens. Actuators A Phys. 47 (1995) 491–493, https://doi.org/10.1016/0924-4247(94)00948-H.

[6] M. Penza, G. Cassano, Relative humidity sensing by PVA-coated dual resonator SAW oscillator, Sens. Actuators B Chem. 68 (2000) 300–306, https://doi.org/10.1016/S0925-4005(00)00448-2.

[7] K.A. Vetelino, P.R. Story, R.D. Mileham, D.W. Galipeau, Improved dew point measurements based on a SAW sensor, Sens. Actuators B Chem. 35 (1996) 91–98, https://doi.org/10.1016/S0925-4005(96)02020-5.

[8] Q. Qi, T. Zhang, Q. Yu, R. Wang, Y. Zeng, L. Liu, H. Yang, Properties of humidity sensing ZnO nanorods-based sensor fabricated by screen-printing, Sens. Actuators B Chem. 133 (2008) 638–643, https://doi.org/10.1016/j.snb.2008.03.035.

[9] T. Fei, J. Dai, K. Jiang, H. Zhao, T. Zhang, Stable cross-linked amphiphilic polymers from a one-pot reaction for application in humidity sensors, Sens. Actuators B Chem. 227 (2016) 649–654, https://doi.org/10.1016/j.snb.2016.01.038.

[10] Y. Li, M.J. Yang, Y. She, Humidity sensors using in situ synthesized sodium polystyrenesulfonate/ZnO nanocomposites, Talanta 62 (2004) 707–712, https://doi.org/10.1016/j.talanta.2003.09.011.

[11] N. Rezlescu, E. Rezlescu, P.D. Popa, F. Tudorache, A model of humidity sensor with a Mg-based ferrite, J. Optoelectron. Adv. Mater. 7 (2005) 907–910.

[12] A. Kassas, J. Bernard, C. Lelièvre, D. Houivet, H. Lakiss, T. Hamieh, Humidity sensitive characteristics of porous Li-Mg-Ti-O-F ceramic materials, Am. J. Anal. Chem. 4 (2013) 83–89, https://doi.org/10.4236/ajac.2013.42011.

[13] Q. Kuang, C. Lao, Z.L. Wang, Z. Xie, L. Zheng, High-sensitivity humidity sensor based on a single SnO_2 nanowire, J. Am. Chem. Soc. 129 (2007) 6070–6071, https://doi.org/10.1021/ja070788m.

[14] R.K. Kotnala, J. Shah, B. Singh, H. Kishan, S. Singh, S.K. Dhawan, A. Sengupta, Humidity response of Li-substituted magnesium ferrite, Sens. Actuators B Chem. 129 (2008) 909–914, https://doi.org/10.1016/j.snb.2007.10.002.

[15] V. Manikandan, S. Sikarwar, B.C. Yadav, S. Vigneselvan, R.S. Mane, J. Chandrasekaran, A. Mirzaei, Rapid humidity sensing activities of lithium-substituted copper-ferrite (Li–$CuFe_2O_4$) thin films, Mater. Chem. Phys. 229 (2019) 448–452, https://doi.org/10.1016/j.matchemphys.2019.03.043.

[16] M.G. Naseri, E.B. Saion, H.A. Ahangar, A.H. Shaari, Fabrication, characterization, and magnetic properties of copper ferrite nanoparticles prepared by a simple, thermal-treatment method, Mater. Res. Bull. 48 (2013) 1439–1446, https://doi.org/10.1016/j.materresbull.2012.12.039.

[17] R.P. Patil, A.D. Pinjarkar, D.J. Sathe, A.S. Chavan, S.D. Delekar, P.P. Hankare, Cation distribution and magnetic study of Cr-substituted lithium ferrites, J. Mater. Sci. Mater. Electron. 27 (2016) 1574–1581, https://doi.org/10.1007/s10854-015-3926-y.

[18] S.M. Patange, S.E. Shirsath, B.G. Toksha, S.S. Jadhav, K.M. Jadhav, Electrical and magnetic properties of Cr^{3+} substituted nanocrystalline nickel ferrite, J. Appl. Phys. 106 (2009) 023914, https://doi.org/10.1063/1.3176504.

[19] G. Raju, N. Murali, M.S.N.A. Prasad, B. Suresh, D. Apparao Babu, M. Gnana Kiran, A. Ramakrishna, M. Tulu Wegayehu, B. Kishore Babu, Effect of chromium substitution on the structural and magnetic properties of cobalt ferrite, Mater. Sci. Energy Technol. 2 (2019) 78–82, https://doi.org/10.1016/j.mset.2018.11.001.

[20] V. Jeseentharani, M. George, B. Jeyaraj, A. Dayalan, K.S. Nagaraja, Synthesis of metal ferrite (MFe_2O_4, M = Co, Cu, Mg, Ni, Zn) nanoparticles as humidity sensor materials, J. Exp. Nanosci. 8 (2013) 358–370, https://doi.org/10.1080/17458080.2012.690893.

[21] L. Greenspan, Humidity fixed points of binary saturated aqueous solutions, J. Res. Natl. Bur. Stand. A Phys. Chem. 81 (1977) 89–96, https://doi.org/10.6028/jres.081A.011.

[22] D.R. Lide. CRC Handbook of Chemistry and Physics, 85th ed., CRC Press, Boca Raton, 2004.

[23] Y. Kumar, A. Sharma, M.P. Shirage, Shape-controlled $CoFe_2O_4$ nanoparticles as an excellent material for humidity sensing, RSC Adv. 7 (2017) 55778–55785, https://doi.org/10.1039/c7ra11072c.

[24] A.M. Dumitrescu, G. Lisa, A.R. Iordan, F. Tudorache, I. Petrila, A.I. Borhan, M. N. Palamaru, C. Mihailescu, L. Leontie, C. Munteanu, Ni ferrite highly organized as humidity sensors, Mater. Chem. Phys. 156 (2015) 170–179, https://doi.org/10.1016/j.matchemphys.2015.02.044.

[25] V.B. Kawade, G.K. Bichile, K.M. Jadhav, X-ray and infrared studies of chromium substituted magnesium ferrite, Mater. Lett. 42 (2000) 33–37, https://doi.org/10.1016/S0167-577X(99)00155-X.

[26] R.G. Dorik, K.B. Modi, K.M. Jadhav, Effect of Cr^{3+} substitution on some physical properties of $CdFe_2O_4$, Indian. J. Pure Appl. Phys. 35 (1997) 594–597.

[27] M. Zeshan, M. Zeeshan, E.-S.M. Sherif, M.Z. Ansari, H.M.T. Farid, Synergistic enhancement of electromagnetic wave absorbance in spinel ferrite–polypyrrole composites, Appl. Nanosci. 13 (2023) 4651–4659, https://doi.org/10.1007/s13204-023-02827-0.

[28] P.R. Chaudhari, D.V. Ahire, V.D. Ahire, M. Chkravarty, S. Maity, Soil bulk density as related to soil texture, organic matter content and available total nutrients of Coimbatore soil, Int. J. Sci. Res. Publ. 3 (2013) 1–8.

[29] S.H. Khoreem, A.H. Al-Hammadi, Enhancing optical properties of Ba-Ni ferrite through nonmagnetic ion doping for sustainable green technologies and renewable energy applications, Discov. Sustain. 5 (2024) 354, https://doi.org/10.1007/s43621-024-00559-x.

[30] H. Riaz, S. Anjum, S.R. Ejaz, M.I. Khan, A. Shanableh, R. Luque, Multifunctional Co^{2+} and Cr^{3+} substituted Ni-Cu spinel ferrites for wastewater remediation and supercapacitor applications, Results Eng. 25 (2025) 104209, https://doi.org/10.1016/j.rineng.2025.104209.

[31] E. Burstein, Anomalous optical absorption limit in InSb, Phys. Rev. 93 (1954) 632–633, https://doi.org/10.1103/PhysRev.93.632.

[32] N. Rajeswari Yogamalar, A. Chandra Bose, Burstein–Moss shift and room temperature near-band-edge luminescence in lithium-doped zinc oxide, Appl. Phys. A 103 (2011) 33–42, https://doi.org/10.1007/s00339-011-6304-5.

[33] M.A.M. Khan, S. Kumar, M.N. Khan, M. Ahamed, A.S. Al Dwayyan, Microstructure and blueshift in optical band gap of nanocrystalline $Al_xZn_{1-x}O$ thin films, J. Lumin. 155 (2014) 275–281, https://doi.org/10.1016/j.jlumin.2014.06.007.

[34] Y. Ammaih, A. Lfakir, B. Hartiti, A. Ridah, P. Thevenin, M. Siadat, Structural, optical and electrical properties of ZnO:Al thin films for optoelectronic applications, Opt. Quantum Electron. 46 (2014) 229–234, https://doi.org/10.1007/s11082-013-9757-2.

[35] R.B. Kale, C.D. Lokhande, Influence of air annealing on the structural, optical and electrical properties of chemically deposited CdSe nano-crystallites, Appl. Surf. Sci. 223 (2004) 343–351, https://doi.org/10.1016/j.apsusc.2003.09.022.

[36] N. Kislov, S.S. Srinivasan, Y. Emirov, E.K. Stefanakos, Optical absorption red and blue shifts in $ZnFe_2O_4$ nanoparticles, Mater. Sci. Eng. B 153 (2008) 70–77, https://doi.org/10.1016/j.mseb.2008.10.032.

[37] A. Manikandan, J.J. Vijaya, M. Sundararajan, C. Meganathan, L.J. Kennedy, M. Bououdina, Optical and magnetic properties of Mg-doped $ZnFe_2O_4$ nanoparticles prepared by rapid microwave combustion method, Superlattices Microstruct. 64 (2013) 118–131, https://doi.org/10.1016/j.spmi.2013.09.021.

[38] M. Junaid, H.A. Jan, K.M. Batoo, R. Jabeen, S. Hussain, Band–gap reduction of aluminum substituted M−type hexagonal ferrite to study its characteristics, Results Chem. 6 (2023) 101133, https://doi.org/10.1016/j.rechem.2023.101133.

[39] E. Poonia, P.K. Mishra, V. Kiran, J. Sangwan, R. Kumar, P.K. Rai, V.K. Tomer, Aerogel assisted synthesis of anatase TiO_2 nanoparticles for humidity sensing application, Dalton Trans. 47 (2018) 6293–6298, https://doi.org/10.1039/C8DT00106E.

[40] V. Manikandan, F. Tudorache, I. Petrila, R.S. Mane, V. Kuncser, B. Vasile, D. Morgan, S. Vigneselvan, A. Mirzaei, Fabrication and characterization of Ru-doped $LiCuFe_2O_4$ nanoparticles and their capacitive and resistive humidity sensor applications, J. Magn. Magn. Mater. 474 (2019) 563–569, https://doi.org/10.1016/j.jmmm.2018.11.072.

[41] A. Mirzaei, K. Janghorban, B. Hashemi, M. Bonyani, S.G. Leonardi, G. Neri, Highly stable and selective ethanol sensor based on α-Fe_2O_3 nanoparticles prepared by Pechini sol–gel method, Ceram. Int. 42 (2016) 6136–6144, https://doi.org/10.1016/j.ceramint.2015.12.176.

[42] D.D. Hawn, B.M. DeKoven, Deconvolution as a correction for photoelectron inelastic energy losses in the core level XPS spectra of iron oxides, Surf. Interface Anal. 10 (1987) 63–74, https://doi.org/10.1002/sia.740100203.

[43] A. Lahiri, N. Borisenko, A. Borodin, M. Olschewski, F. Endres, Characterisation of the solid electrolyte interface during lithiation/delithiation of germanium in an ionic liquid, Phys. Chem. Chem. Phys. 18 (2016) 5630–5637, https://doi.org/10.1039/C5CP06184A.

[44] C. Calderón, P. Bartolo-Pérez, O. Rodríguez, G. Gordillo, Phase identification and XPS studies of Cu(In,Ga)Se_2 thin films, Microelectron. J. 39 (2008) 1324–1326, https://doi.org/10.1016/j.mejo.2008.01.071.

[45] M.T. Marques, A.M. Ferraria, J.B. Correia, A.M.B. do Rego, R. Vilar, XRD, XPS and SEM characterisation of Cu–NbC nanocomposite produced by mechanical alloying, Mater. Chem. Phys. 109 (2008) 174–180, https://doi.org/10.1016/j.matchemphys.2007.10.032.

[46] M. Zhu, T.C.R. Rocha, T. Lunkenbein, A. Knop-Gericke, R. Schlögl, I.E. Wachs, Promotion mechanisms of iron oxide-based high temperature water–gas shift

catalysts by chromium and copper, ACS Catal. 6 (2016) 4455–4464, https://doi.org/10.1021/acscatal.6b00698.

[47] N. Himansulal, Kinetics study on the thermal decomposition of lanthanum oxalate catalysed by Zn-Cu nano ferrites, Res. J. Mater. Sci. 3 (2015) 1–8.

[48] Y. Shen, Y. Wu, H. Xu, J. Fu, X. Li, Q. Zhao, Y. Hou, Facile preparation of sphere-like copper ferrite nanostructures and their enhanced visible-light-induced photocatalytic conversion of benzene, Mater. Res. Bull. 48 (2013) 4216–4222, https://doi.org/10.1016/j.materresbull.2013.06.063.

[49] R.K. Swarnkar, S.C. Singh, R. Gopal, Effect of aging on copper nanoparticles synthesized by pulsed laser ablation in water: structural and optical characterizations, Bull. Mater. Sci. 34 (2011) 1363–1369, https://doi.org/10.1007/s12034-011-0329-4.

[50] R. Shunmuga Priya, P. Chaudhary, E. Ranjith Kumar, A. Balamurugan, C. Srinivas, G. Prasad, B.C. Yadav, D.L. Sastry, Evaluation of structural, dielectric and electrical humidity sensor behaviour of $MgFe_2O_4$ ferrite nanoparticles, Ceram. Int. 47 (2021) 15995–16008, https://doi.org/10.1016/j.ceramint.2021.02.174.

[51] M.E. Rabanal, A. Várez, B. Levenfeld, J.M. Torralba, Magnetic properties of Mg-ferrite after milling process, J. Mater. Process. Technol. 143–144 (2003) 470–474, https://doi.org/10.1016/S0924-0136(03)00464-3.

[52] K.B. Modi, Elastic moduli determination through IR spectroscopy for zinc substituted copper ferri chromates, J. Mater. Sci. 39 (2004) 2887–2890, https://doi.org/10.1023/B:JMSC.0000021472.00590.9b.

[53] J. Smit, H.P.J. Wijn, Ferrites, Philips Technical Library, Eindhoven, The Netherlands, 1959.

[54] W. Qu, W. Wlodarski, J.-U. Meyer, Comparative study on micromorphology and humidity sensitive properties of thin-film and thick-film humidity sensors based on semiconducting $MnWO_4$, Sens. Actuators B Chem. 64 (2000) 76–82, https://doi.org/10.1016/S0925-4005(99)00487-6.

[55] P.K. Kannan, D.J. Late, H. Morgan, C.S. Rout, Recent developments in 2D layered inorganic nanomaterials for sensing, Nanoscale 7 (2015) 13293–13312, https://doi.org/10.1039/C5NR03633J.

[56] A.S. Pawbake, R. Waykar, D.J. Late, S.R. Jadkar, Highly transparent wafer-scale synthesis of crystalline WS_2 nanoparticle thin film for photodetector and humidity-sensing applications, ACS Appl. Mater. Interfaces 8 (2016) 3359–3365, https://doi.org/10.1021/acsami.5b11325.

[57] J. Herrán, I. Fernández, E. Ochoteco, G. Cabañero, H. Grande, Sens. Actuators B Chem. 198 (2014) 239–242, https://doi.org/10.1016/j.snb.2014.03.043.

[58] V.K. Tomer, S. Thangaraj, S. Gahlot, K. Kailasam, Cubic mesoporous Ag@CN: a high performance humidity sensor, Nanoscale 8 (2016) 19794–19803, https://doi.org/10.1039/c6nr08039a.

[59] K. Manjunatha, B. Chethan, S.Y. Wu, M. Ubaidullah, S.F. Shaikh, A.M. Al-Enizi, N. B. Alanazi, B. Pandit, A. Bajorek, V.J. Angadi, Effect of Eu^{3+} and Sc^{3+} on the structure, microstructure and humidity sensing properties of copper ferrites for sensor applications, Ceram. Int. 49 (2023) 40236–40243, https://doi.org/10.1016/j.ceramint.2023.09.359.

[60] V.J. Angadi, K. Manjunatha, M.-K. Ho, S.Y. Wu, M. Ubaidullah, A.M. Al-Enizi, B. Pandit, B. Chethan, X-ray photoelectron spectroscopy, Raman and humidity sensing properties of Sm^{3+} doped $CoCr_2O_4$ for humidity sensor applications, J. Inorg. Organomet. Polym. Mater. 34 (2024) 1712–1724, https://doi.org/10.1007/s10904-023-02912-5.

[61] C.D. Hatch, J.S. Wiese, C.C. Crane, K.J. Harris, H.G. Kloss, J. Baltrusaitis, Water adsorption on clay minerals as a function of relative humidity: application of BET and Freundlich adsorption models, Langmuir 28 (2012) 1790–1803, https://doi.org/10.1021/la2042873.

[62] A. Sharma, P. Bhojane, A.K. Rana, Y. Kumar, P.M. Shirage, Mesoporous nickel cobalt hydroxide/oxide as an excellent room temperature ammonia sensor, Scr. Mater. 128 (2017) 65–68, https://doi.org/10.1016/j.scriptamat.2016.10.003.

[63] J. Huang, Q. Wan, Gas sensors based on semiconducting metal oxide one-dimensional nanostructures, Sensors 9 (2009) 9903–9924, https://doi.org/10.3390/s91209903.

Tripti Mandal received her Master's degree in Physics from Government M.V.M., Bhopal, affiliated with Barkatullah Vishwavidyalaya, Bhopal, India. She is currently pursuing a Ph. D. in Physics at Fergusson College (Autonomous), Pune, affiliated with Savitribai Phule Pune University (SPPU), India. She is serving as an Assistant Professor of Physics in the Department of Engineering Sciences at Zeal College of Engineering and Research, Narhe, Pune. Her research focuses on ferrite materials and their applications in humidity sensing.

Yesappa D. Kolekar is a Professor in the Department of Physics at Savitribai Phule Pune University, Pune, India. He obtained his Ph.D. from Shivaji University, Kolhapur. His research focuses on magnetic materials and multiferroic materials.

Rakesh A. Afre is an Associate Professor at the School of Technology and Research, Dyaan Prasad Global University, Pune, India. He holds an M.Sc. in Physics from North Maharashtra University and a Ph.D. in Nanotechnology from the Nagoya Institute of Technology, Japan. His research focuses on nanomaterials for energy applications, with particular expertise in organic and perovskite solar cells, as well as advanced electrochemical devices. Dr. Afre has authored over 35 peer-reviewed publications, along with 2 books, 5 book chapters, and holds two international patents. He brings extensive international research experience, having collaborated with leading institutions including the Nagoya Institute of Technology (Japan), KRICT (South Korea), Flinders University (Australia), and Jimma University (Ethiopia). In addition to his research, he actively contributes to the scientific community as a reviewer and editorial board member for several reputed international journals. Dr. Afre also serves as an international expert and reviewer in nanotechnology for UEFISCDI (Romania) and the Technology Agency of the Czech Republic (TACR).

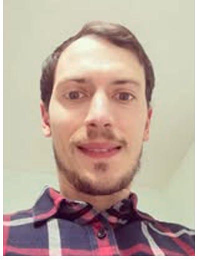

Diego Pugliese earned his Ph.D. in Physics from the Polytechnic University of Turin in 2014. He then pursued post-doctoral research at the Department of Applied Science and Technology, specializing in the synthesis and characterization of non-silica oxide-based glasses for photonics and bio-photonics. Since July 2023, he is a researcher at the National Institute of Metrological Research (INRiM), Italy, focusing on novel materials, processes, devices, and systems supporting the Clean Energy Transition. He has authored over 100 papers in international journals and is co-inventor of an Italian patent.

Kishor M. Sonawane is a Professor of Physics in the Department of Physics at Fergusson College (Autonomous), Pune, affiliated with Savitribai Phule Pune University, India. He received his Ph.D. in 2006 from Swami Ramanand Tirth Marathwada University, Nanded, India. His research focuses on the synthesis of thin films and their applications in gas sensing and solar cells.